Angewandte Chemie
Eine Zeitschrift der Gesellschaft Deutscher Chemiker

Supporting Information

Current-Density Regulating Lithium Metal Directional Deposition for Long Cycle-Life Li Metal Batteries

*Heng Mao, Wei Yu, Zhuanyun Cai, Guixian Liu, Limin Liu, Rui Wen, Yaqiong Su, Huari Kou, Kai Xi, Benqiang Li, Hongyang Zhao, Xinyu Da, Hu Wu, Wei Yan, and Shujiang Ding**

anie_202105831_sm_miscellaneous_information.pdf

Methods

Preparation of CCA. Medical-grade cotton ball was used as the cellulose. All other reagents were analytical grade and used without further purification. Medical-grad cotton balls were dispersed in NaOH aqueous solution (Cellulose/NaOH/deionized water: 2 wt%/12 wt%/86 wt%). Then it was placed at a low temperature of -15 ^{o}C overnight. The treated cellulose was added to a graphene oxide solution (GO, 2 mg/ml) with the content of cellulose in the GO/cellulose powder mixture ratio of 10 wt%. The solution was then stirred by strong mechanical rabbling. Then the mixed solution was then put into a culture dish and gelated by standing at room temperature. Excess NaOH was removed by soaking in 5% acetic acid aqueous solution. A Freeze-drying technique was used to remove the water and prepared the final cellulose-based graphene oxide composite aerogel. Finally, CCA was prepared by 900 ^{o}C high-temperature pyrolysis for 2 h in argon at a heating rate of 2 ^{o}C min^{-1}. The density of CCA was calculated to be 0.028 g cm^{-3} (Table S3).

Preparation of LCL-melting electrode. To modify the lithium affinity of CCA, CCA was soaked in zinc acetate water solution (40 mg/ml) for 12 h. Then CCA@ZnO composite was sintered at 600 ^{o}C pyrolysis for 2 h. The morphology characterization is shown in Fig. S21. Next, polished Li foil was placed on the top of CCA@ZnO composite and melted at 350 ^{o}C in the glovebox, leading to the formation of the LCL-melting electrode.

Material and electrochemical characterizations. Field-emission scanning electron microscopy with mapping (FESEM; Zeiss Gemini 500) was used to observe the morphology and microstructure of the electrodes and CCA. The electrochemical performances of LCL-without, LCL-interlayer, LCL-melting and LCL-bottom electrodes were tested using CR2025-type coin cells which were assembled in an AR-filled glovebox (H_2O and O_2 below 0.1 ppm). Celgard PP membrane was used as the separator. The mixed solution of 1 M lithium bistrifluoromethanesulphonylimide (LiTFSI) in 1, 2-dimethoxyethane (DME) and 1, 3-dioxolane (DOL) (1:1, v/v) with 1.0 % $LiNO_3$ was used as the electrolyte for the symmetric cells. The electrolyte of LFP/Li

and LFP/CCA-Li full cells was 1 M $LiPF_6$ in ethylene carbonate (EC)/diethyl carbonate (DEC) (1:1, v/v)+5 wt% vinylene carbonate (VC). The electrochemical impedance spectroscopy (EIS) cyclic ability was performed using CHI660D electrochemical workstation (CH instruments, Shanghai) and NEWARE battery tester, respectively.

***In situ* OM imaging.** Li foils were used as the working and counter electrodes. The two lithium foil electrodes were fixed on a Teflon disk with an annular tank in the center to hold 1 M lithium bistrifluoromethanesulphonylimide (LiTFSI) in 1, 2-dimethoxyethane (DME) and 1, 3-dioxolane (DOL) (1:1, v/v) with the addition of $LiNO_3$ (1 wt%). Then the disk was enclosed in an airtight container, and a transparent glass window was prearranged on the upper surface of the container. All processes were conducted in the glove box filled with argon. The *in situ* real-time OM imaging was performed by an optical microscope (OLYMPUS, OLS-4000) and the electrochemical station (CHI760E, Chenhua, Shanghai).

DFT calculations. Spin-polarized calculations within the density-functional theory framework were carried out as implemented in the Vienna *ab initio* simulation package (VASP).[S1] The ion-electron interactions were represented by the projector-augmented wave (PAW) method and the electron exchange-correlation by the generalized gradient approximation (GGA) with the Perdew-Burke-Ernzerhof (PBE) exchange-correlation functional.[S2-S3] The Kohn-Sham valence states were expanded in a plane-wave basis set with a cut-off energy of 400 eV. The empirical DFT-D3 correction was contained for the weak van der Waals interaction,[S4] and the dipole correction was also adopted for all calculations.[S5] For graphene supported Li clusters, the model was Li_9 monolayer supported on a (3×3) supercell of graphene and all atoms were allowed to relax. For Li (110) supported graphene, graphene monolayer was covered on Li (110) which was a periodic three-layer slab with a $(2\sqrt{2}\times4)$ surface unit cell, and the atoms in the bottom two layers were frozen to their bulk position, and the rest of the atoms was allowed to relax. For the Brillouin zone integration, an 11×11×1 Monkhorst-Pack mesh was used. The geometry optimization was performed when the convergence criterion on forces became smaller than 0.02 eV/Å, and the energy difference was $<10^{-5}$ eV.

ATK simulation. The simulation of current density was implemented in the

QuantumWise Atomistix Toolkit (ATK-VNL) 2019 program, which is a density-functional theory code using numerical localized atomic basis sets. ATK allows for simulating open systems through the use of a nonequilibrium Green's function (NEGF) formalism.[S6] The PBE-GGA functional was adopted to describe the exchange and correctional interactions of electrons with a linear combination of atomic orbitals (LCAO) norm-conserving PseudoDojo pseudopotential,[S7-S8] which contains scalar relativistic and fully relativistic pseudopotentials for each element and it is shipped with multiple projectors for each angular channel to ensure high accuracy.[S9] A Poisson solver was employed, which combines the fast Fourier transform (FFT) method in the x- and y- directions (in which the structure is periodic) with a multigrid solver for the z- direction,[S10] where Dirichlet boundary conditions are used for the open system. A double-ζ polarized basis set for expanding the electronic density was used for Li and C atoms. The density mesh cut-off of 150 Rydberg and 11 *k* points in the y-direction was adopted for all calculations.

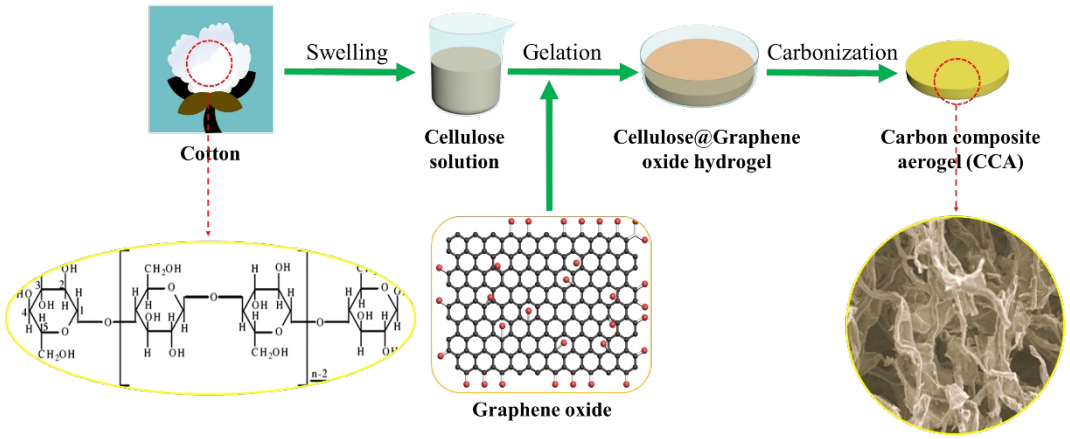

Figure S1. The simple schematic illustration of preparation. CCA was prepared by the mothed of sol-gel. Cotton cellulose as raw material is a polyhydroxy natural polymer.

As shown in Fig. S1, cotton cellulose, a polyhydroxy natural polymer, was used as the raw material. The cellulose-based aerogel was prepared by the sol-gel method. During the synthesis process, hydrogen bonds between the cellulose chains break by vigorous mechanical agitation under low

temperature. And new bonds between the oxygen-containing groups on the GO surfaces and the hydroxyl group of cellulose are formed at room temperature to obtain the Cellulose@Graphene Oxide hydrogel. Finally, CCA was prepared by the method of freeze-drying and high temperature. carbonization.

Figure S2. Digital images of the aerogel at different stages of the preparation. (a, b)

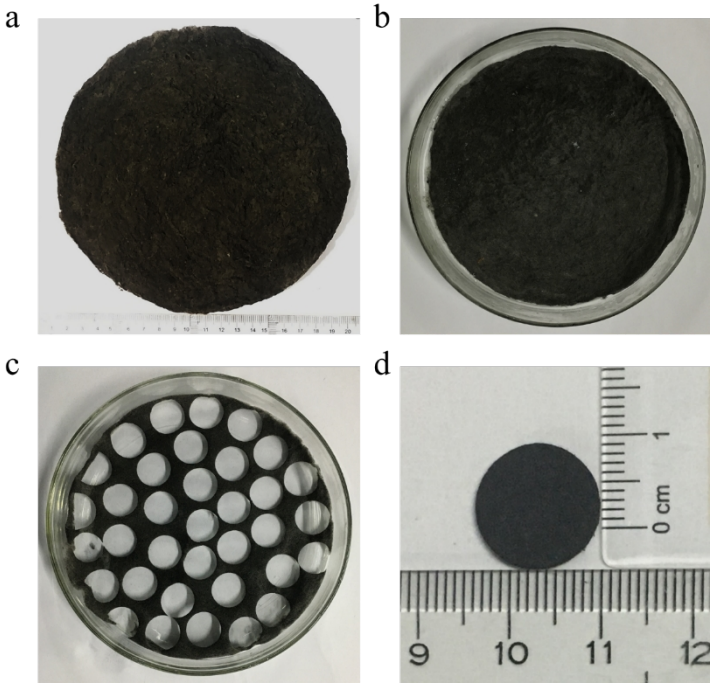

Cellulose@graphene oxide green aerogel. **(c)** Discs of cellulose@graphene oxide aerogel were manufactured by a sheet-punching machine. **(d)** CCA electrode disc after high-temperature carbonization.

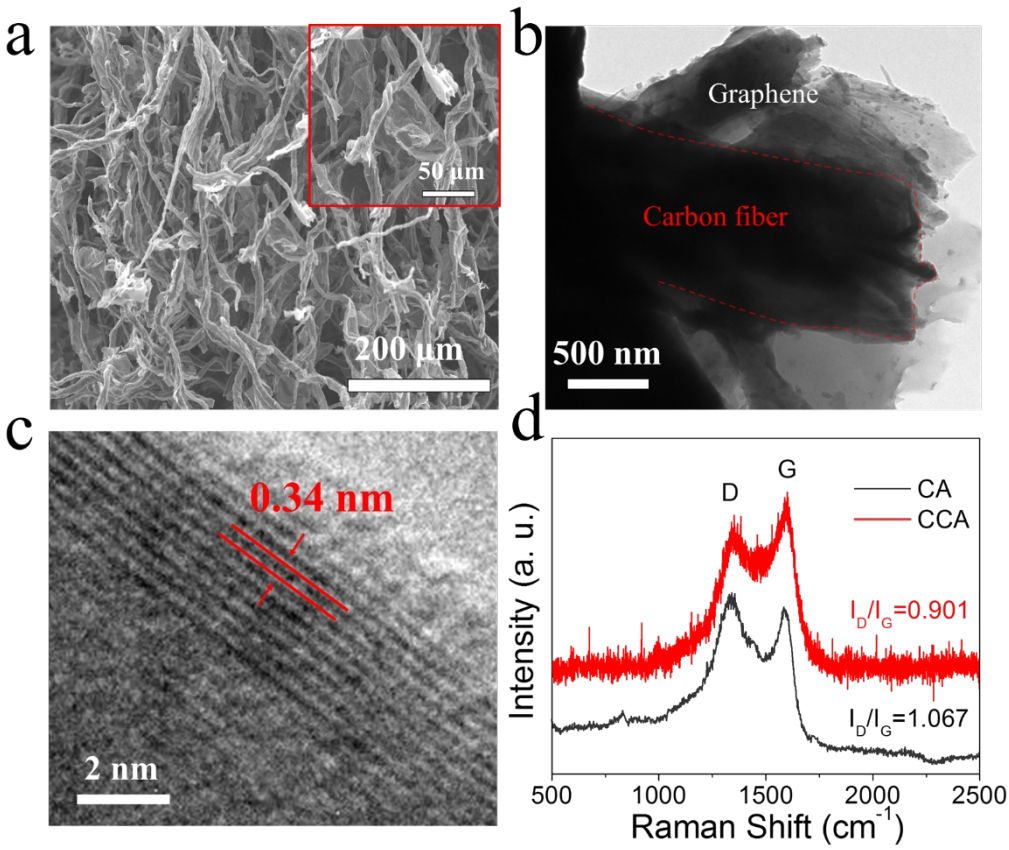

Figure S3. Characterization analysis of cellulose/graphene carbon composite aerogel (CCA). (a, b) The FESEM and TEM images of CCA. (c) The HRTEM image of graphene displays the interlayer spacing of 0.34 nm. (d) Raman spectra of cellulose-based carbon aerogel (CA) and CCA.

Both scanning electron microscope (SEM) and transmission electron microscope (TEM) analyses show that the 3D porosity of CCA is a result of the dual structure of the carbon network, where one-dimensional (1D) nanofibers are well stuck to the two-dimensional (2D) graphene flakes (Fig. S3a, and b). High resolution TEM (HRTEM) images show an interlayer spacing of 0.34 nm (Fig. S3c), indicating the existence of graphene. Raman spectroscopy was carried out to verify the existence of graphene (Fig. S3d). The graphitization degree of CCA (ID/IG is 0.901) is better than that of cellulose-based carbon aerogel (CA; 1.067), because of the addition of graphene oxide.

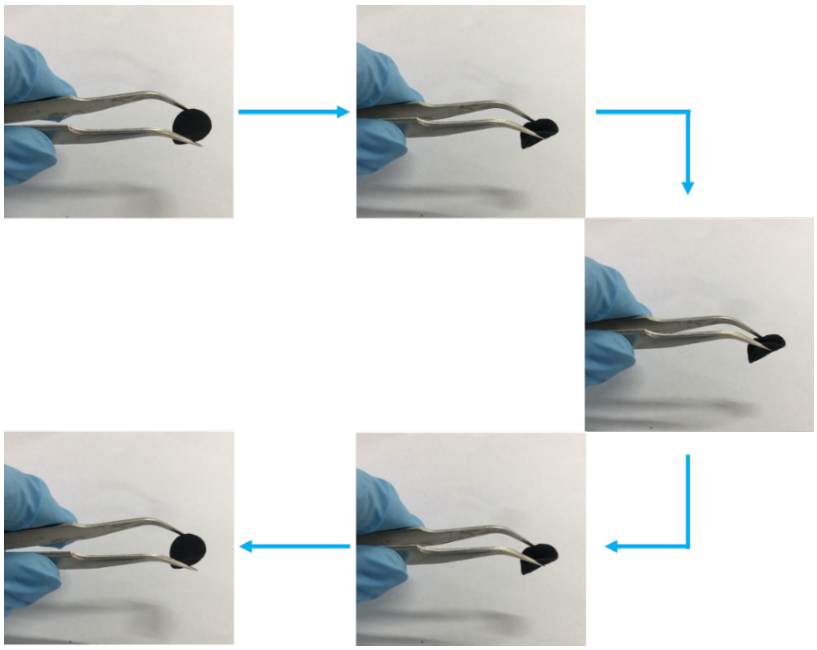

Figure S4. Testing the flexibility and mechanical integrity of CCA. The CCA possess excellent flexibility and can maintain well after folding and stretching.

The mechanical durability and flexibility of the CCA were tested under bending, folding, twisting, and stretching forces; all indicating a robust and integrated structure.

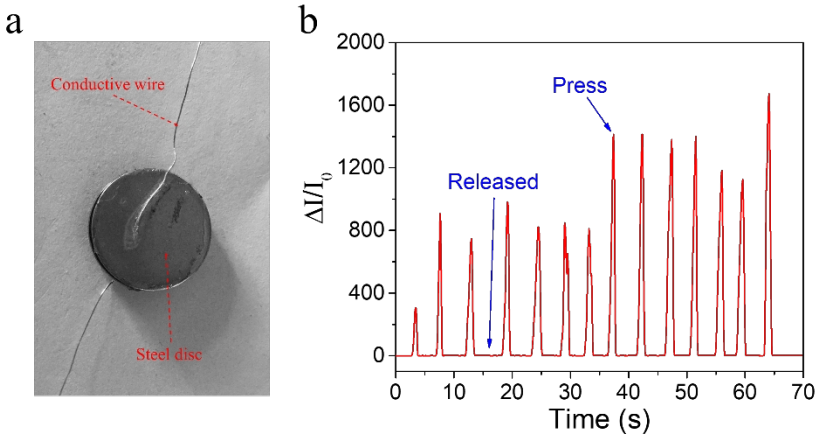

Figure S5. A pressure sensor based on the CCA. (a) Digital image showing the device used in the experiments. **(b)** The current responses of pressure/release cycles measured at 0.01 V. I_0 is the initial current

The CCA compressibility was confirmed by testing it as a pressure sensor, which showed an excellent response to the pressure/release cycle.

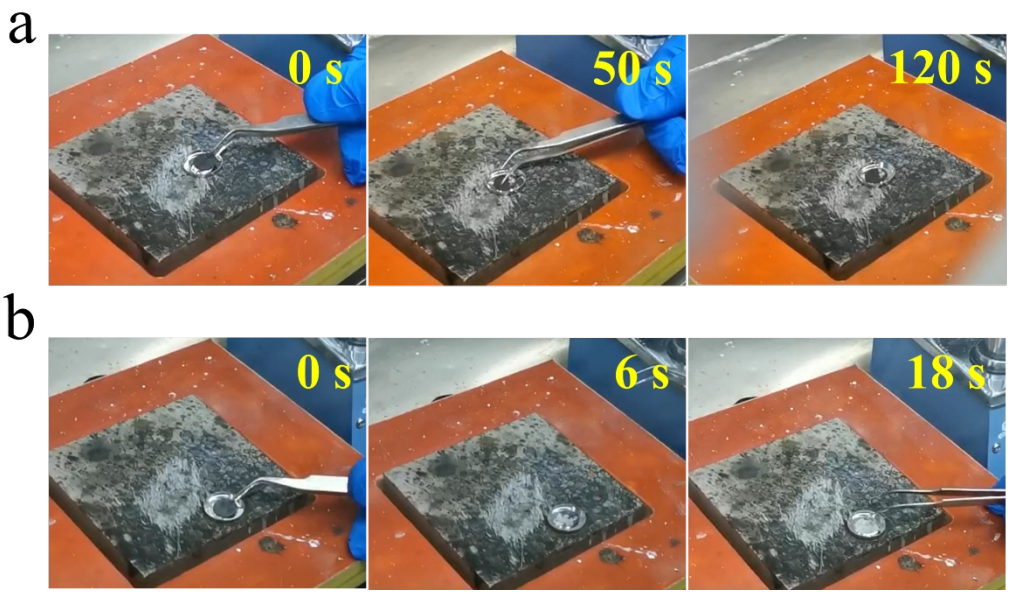

Figure S6. The Li affinity images of **(a)** CCA. **(b)** CCA@ZnO composite material.

As shown in Fig. S6, the rate of molten lithium entering the CCA without ZnO modification is very slow. There is only a small amount of lithium in the CCA after 120s. However, the molten lithium has been completely incorporated into the CCA@ZnO composite materials after only 18s. This may be due to lithiophilic modification of ZnO.

Table S1. Summary of the electrochemical performance of LCL-bottom electrode with different strategies

Strategy	Current density ($mA\ cm^{-2}$)	Capacity ($mAh\ cm^{-2}$)	Cycle number/Overpotential	Reference
LCL-bottom	**10**	**1**	**1000 /~118 mV**	**This work**
Li/C-wood	3	1	225/~150 mV	S11
TiC/C/Li	3	1	200/~85 mV	S12
N-doped graphene-Li	10	1	~180 mV	S13
Li@PNNF	5	1	150/~39 mV	S14
CFC/Li	10	1	200/~170 mV	S15
OP-10 additives	4	1	160/~250 mV	S16
Coating Ag(Au) layer-Li	1	1	425/~85 mV	S17
Li-coated PI-ZnO	5	1	100/~200 mV	S18
Straw-brick-like CFC/Li	5	1	100/~120 mV	S19

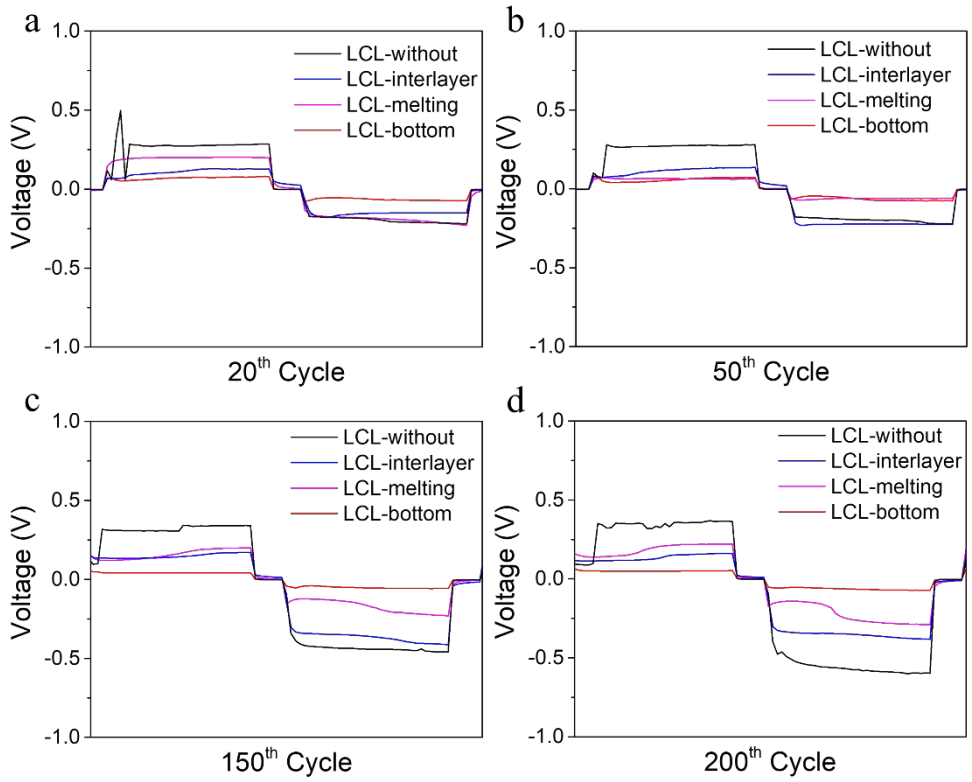

Figure S7. The overpotential of nucleation and stable voltage for the different electrodes after many cycles. (a) 20th cycle. **(b)** 50th cycle. **(c)** 150th cycle. **(d)** 200th cycle. The LCL-bottom cell displays the lowest voltage hysteresis and more most stable voltage than that of the other three cells.

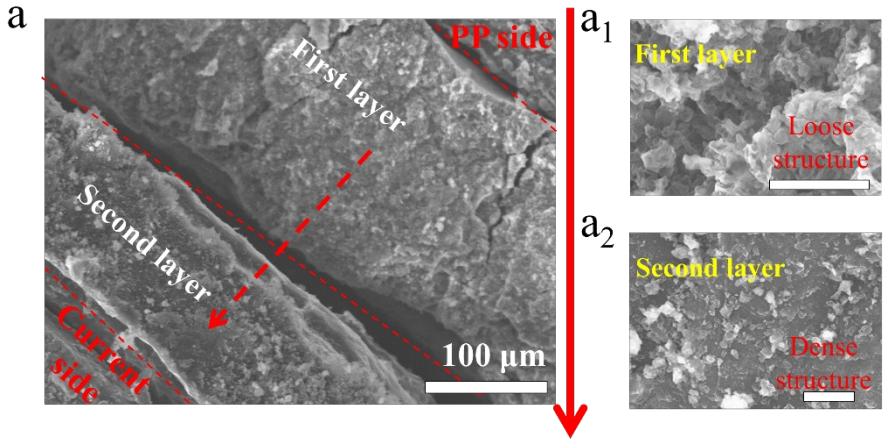

Figure S8. Cross-section SEM of Li metal anodes after cycles in D1 configuration. (a) Overall cross-sectional SEM image of Li metal anodes after cycling. **Local cross-sectional SEM image. (a_1),** The first layer. **(a_2)** The second layer. White scale bars on each image are 5 μm.

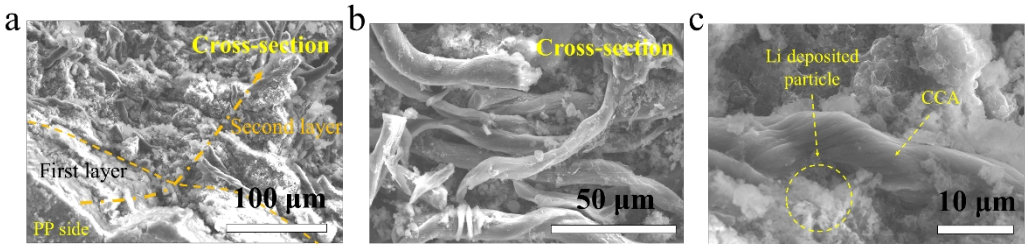

Figure S9. Cross-section SEM of LCL-interlayer electrode after 530 cycles. (a) Overall cross-section SEM image. **(b, c)** SEM images of the second layer.

From the Fig. S9, we can see that the whole LCL-interlayer electrode has been divided into two layers after cycles. The structure of the first layer near the PP separator is lithium deposition particles without carbon fibers. The structure of the second layer is CCA filled with lithium deposition particles. The result just shows that Li metal migrates up gradually, and continue with its original formation of tip-like dendrites.

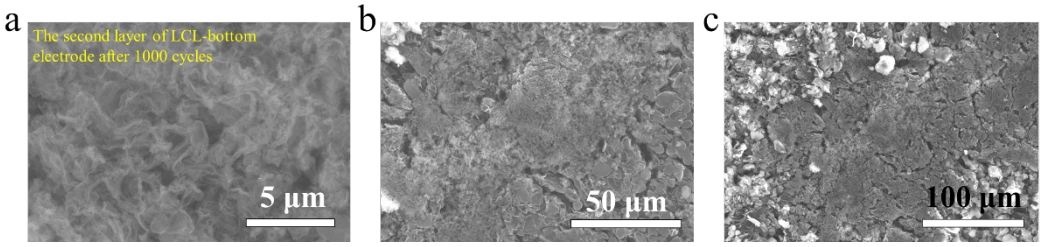

Figure S10. The morphology of the second (middle) layer of the LCL-bottom electrode after 1000 cycles at 10 mA cm^{-2} and 1 mAh cm^{-2}. The second-layer structure of the LCL-bottom electrode is loose and dendritic.

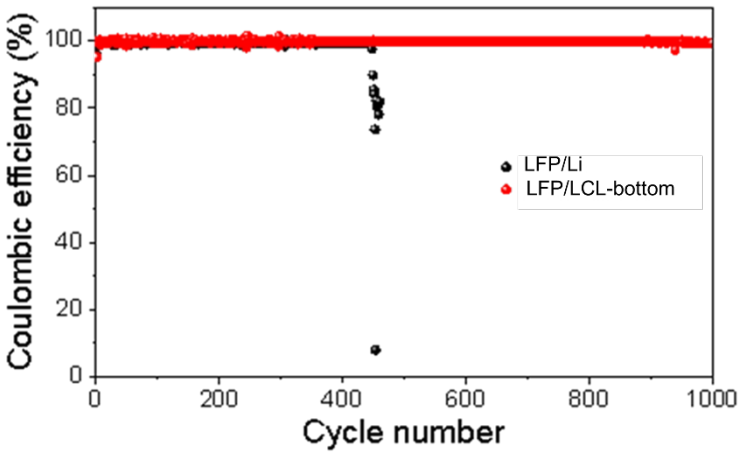

Figure S11. The coulombic efficiency (CE) of the full cell using pure Li and LCL-bottom anodes with commercial $LiFePO_4$ (LFP) as the cathode.

Table S2. Summary of the electrochemical performance of full cell with $LiFePO_4$ (LFP) cathode

Current density	Cycle number	Capacity retention	Reference
1 C	**1000**	**94%**	**This work**
5 C	**1000**	**85%**	
0.5 C	100	90%	S20
1 C	1000	91%	S21
5 C	200	91%	S22
0.5 C	200	91%	S23
0.2 C	500	87%	S24
1 C	100	80%	S25
1 C	500	89%	S26

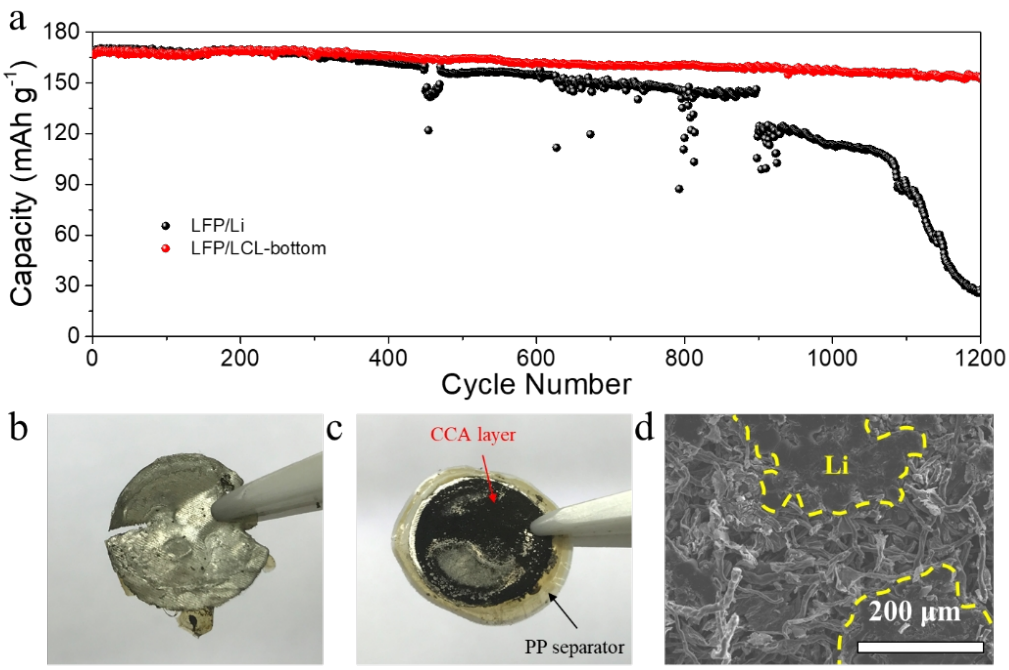

Figure S12. Analysis of pure Li and LCL-bottom anodes after cycling in full cells with commercial $LiFePO_4$ (LFP) as the cathode. (a) Cycling stability of LFP/Li and LFP/ LCL-bottom batteries. **(b)** The Li metal anode bottom image of LFP/Li cell. **(c)** The LCL-bottom image of LFP/ LCL-bottom cell. **(d)** The LCL-bottom anode bottom SEM image.

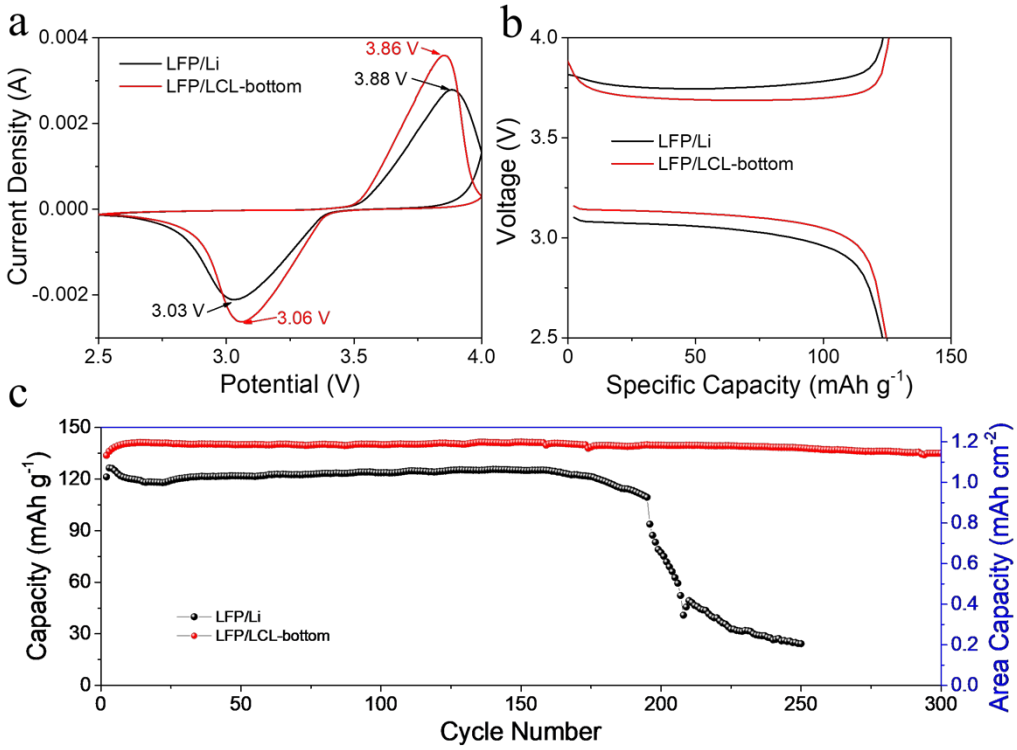

Figure S13. Electrochemical measurements: (a) At a scan rate of 0.2 mV s^{-1}, cyclic voltammograms (CV) of LFP/Li, LFP/LCL-bottom full cells. **(b)** Charge-discharge voltage profiles for three different current collectors at 5 C. **(c)** The cycling behavior of cells that contain pure Li and CCA-Li anodes with $LiFePO_4$ (LFP) cathode at 1 C. The loading is ~9.6 mg cm^{-2}.

The cyclic voltammogram (CV) was carried out at the scan rate of 0.2 mV s^{-1} (Fig. S13a). The oxidation potential and reduction potential for LFP/LCL-bottom full cell is 3.86, and 3.06 V, respectively. The oxidation potential of LFP/LCL-bottom full cell is lower than that of LFP/Li full cell (3.88 V) whereas the reduction potential of LFP/LCL-bottom full cell is higher than that of LFP/Li full cell (3.03 V). Therefore, the LFP/LCL-bottom full cell exhibits a smaller polarization voltage, which is in accord with the galvanostatic charge/discharge performed at 5 C (Fig. S13b). We also tested it by using a commercial LFP cathode with ~9.60 mg loading (Fig. S13c). The LFP/LCL-bottom cell showed outstanding cyclic performance with about 1.13 mAh cm^{-2} of initial areal capacity at 1 C. The capacity retention of the LFP/LCL-bottom cell was approximately 96 % of its highest value after 300 cycles compared with that of LFP/Li cell (approximately 19 % of its highest value after 250 cycles).

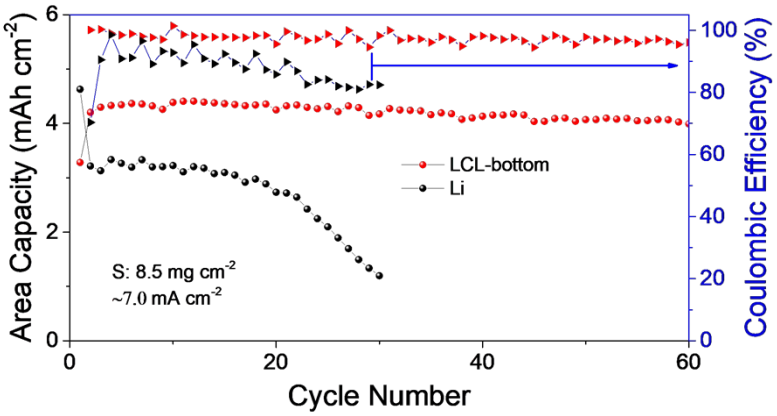

Figure S14. Cycling performance of LCL-bottom and pure Li at the current density of ~7.0 mA cm^{-2} with ~8.5 mg cm^{-2} S loading. The area capacity could keep more than 4.0 mAh cm^{-2}.

Finally, the cycle performance of LCL-bottom with S cathode was tested at ~7.0 mA cm^{-2} with 8.5 mg S loading and electrolyte/sulfur (E/S) ratio of ~9.0 μL mg^{-1}, as shown in Fig. S14. The areal capacity could maintain more than 4.0 mAh cm^{-2}, which is better than that of pure Li with S cell (Fast decay to ~1.2 mAh cm^{-2}).

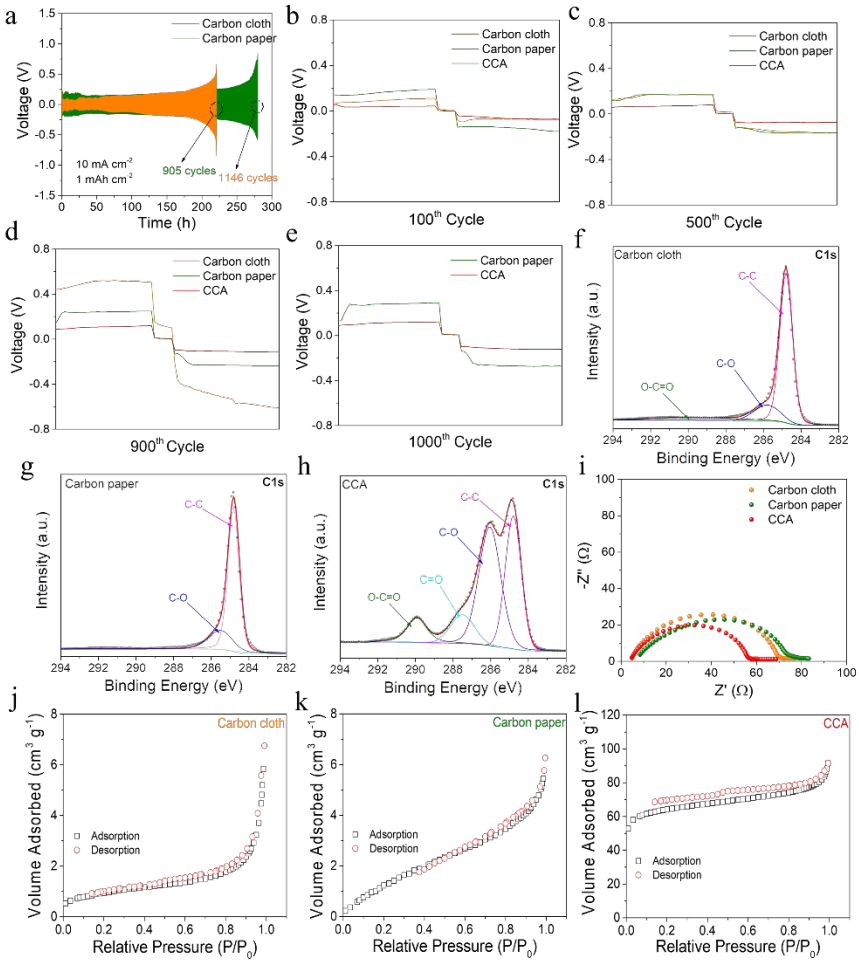

Figure S15. (a) Cycling stability of cell with CCA replaced by commercial carbon cloth and carbon paper. Overpotential and stable voltage after many cycles. **(b)** 100th cycle. **(c)** 500th cycle. **(d)** 900th cycle. **(e)** 1000th cycle. **The C 1s peaks of. (f)** Carbon cloth. **(g)** Carbon paper. **(h)** CCA. **(i)** AC impedance curve of carbon cloth, carbon paper and CCA. **N_2 adsorption-desorption isotherms. (j)** Commercial carbon cloth. **(k)** Commercial carbon paper. **(l)** CCA. The specific surface of carbon cloth, carbon paper and CCA were calculated to be 3.38, 6.53 and 204.55 m^2 g^{-1}, respectively.

Fig. S15b, c and d show the voltage profiles of the three-electrode types at the 100th, 500th, and 900th cycles. The overpotential of the LCL-bottom electrode was comparable to that of the other carbon electrode up to the first 500 cycles. However, for longer cycling, LCL-bottom displayed a lower nucleation overpotential and more stable voltage than the other two carbon materials (Fig. S15e). It is worth noting that the overpotential of the carbon cloth-Li electrode was higher than that of the carbon cloth-Li electrode during the first 100 cycles, but the stability of the carbon paper-Li

electrode seemed to improve by cycling. To explore these reasons, X-ray photoelectron spectroscopy (XPS) measurements were carried out. As shown in Fig. S15f, g, h. The C 1s peaks of CCA can be assigned to C-C (284.8 eV), C-O (286.1 eV), C=O (287.5 eV), and O-C=O (289.9 eV) bonds. The C 1s of carbon cloth contains C-C (284.8 eV), C-O (285.8 eV), and O-C=O (289.6 eV) bonds. The C 1s of carbon paper contains only C-C (284.8 eV) and C-O (285.6 eV) bonds. CCA has more oxygen functional groups on its surface than both carbon paper and carbon cloth. These oxygen-containing groups could work as seeds for the Li nucleation, leading to the more facile deposition of Li. In addition, the oxygen groups link the deposited Li and the carbon backbone of the CCA, improving the adhesion between them. Therefore, the overpotential of CCA is lower than that of other carbon materials. Similarly, the initial lower overpotential of carbon cloth compared with carbon paper is due to the popularity of the oxygen functional groups on its surface. Meanwhile, Nyquist plots were obtained to investigate the electronic conductivity of the electrodes (Fig. S15i). The results indicate that the conductivity of LCL-bottom was the best, and that the conductivity of carbon cloth-Li was better than that of carbon paper-Li. Hence, the better electrical conductivity of the electrodes would also lead to a lower nucleation overpotential.

However, the nucleation overpotential of carbon cloth-Li was higher than that of carbon paper-Li after 500 cycles. We believe that the long cycle stability is affected by the size of the Li metal deposition space. To explore the reasons, N_2 adsorption/desorption isotherms were obtained (Fig. S15j, k, l). All carbon materials showed type IV according to the IUPAC, with some hysteresis loops in the medium to high-pressure regions, indicating the presence of mesopores. CCA has the largest specific surface area (204.55 $m^2\ g^{-1}$), and that of carbon cloth (3.38 $m^2\ g^{-1}$) is the smallest (that of carbon paper is 6.53 $m^2\ g^{-1}$). This large surface not only facilitates interaction with the electrolyte, but also satisfies a more homogeneous charge distribution on the Li metal anode surface, thereby decreasing the possibility of dendrite formation. Hence, the conductivity and electrochemical activity of the electrodes determine the initial nucleation overpotential and the specific surface area is the key factor for the long cycle

stability. The unique surface and morphological properties of CCA provide numerous Li deposition sites and are helpful to maintain good contact between the individual Li particles to ensure a percolation pathway for both ions and electrons.

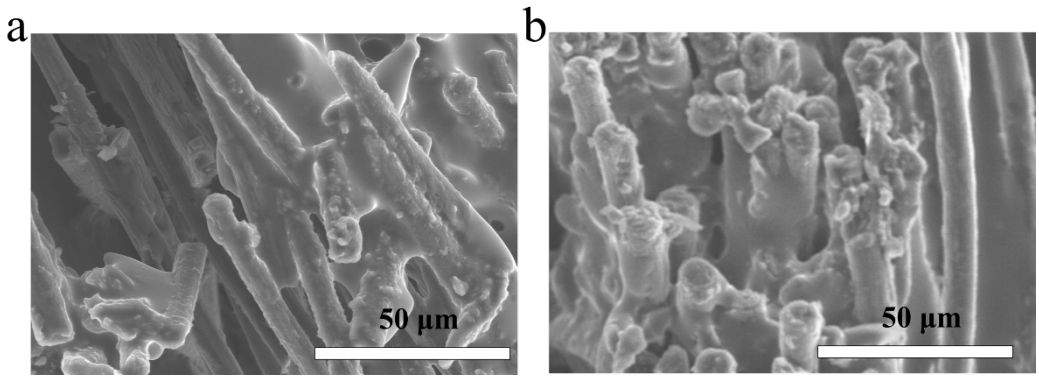

Figure S16. The cross-section SEM images of (a) commercial carbon paper. **(b)** commercial carbon cloth.

As shown in Fig. S16, Li deposition also occurs in commercial carbon and carbon cloth. Indicating commercial carbon and carbon cloth can also be used as lithium metal deposition sites. Therefore, this strategy can also be applied to commercial carbon cloth and carbon paper.

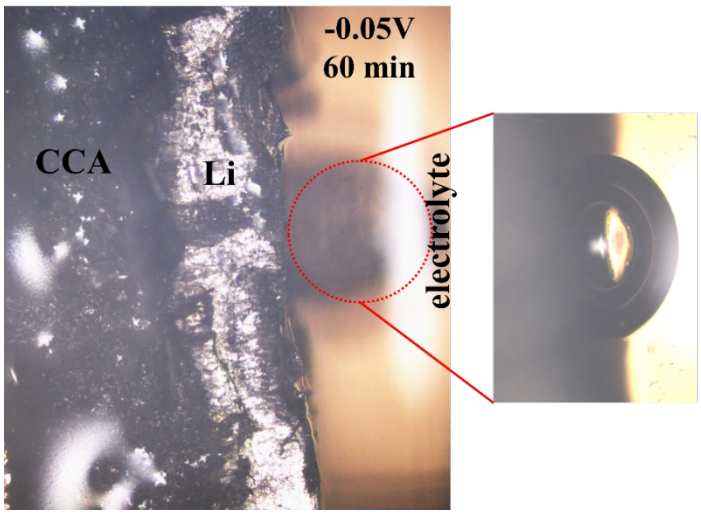

Figure S17. Li morphology of LCL-bottom electrode at the anode/electrolyte interface upon Li deposition at -0.05 V for 60 min and local magnification image.

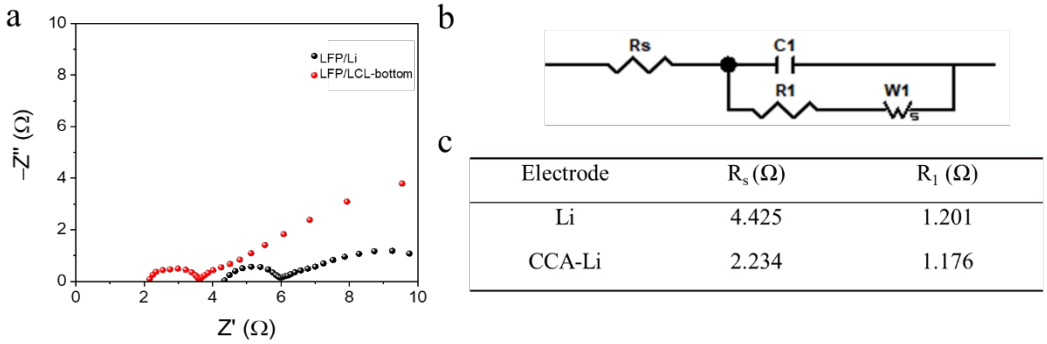

Electrode	R_s (Ω)	R_1 (Ω)
Li	4.425	1.201
CCA-Li	2.234	1.176

Figure S18. Electrochemical impedance spectroscopy analysis of pure Li and LCL-bottom after 10 cycles. (a) the Nyquist plots. **(b)** an equivalent circuit model. **(c)** parameter values of the equivalent circuits.

R_s is the resistance from the deposition point to the collector along the electron channel, which is related to the electronic conductivity of the anode; R_{Li} is the Li-ion transport resistance; and R_{ct} is the charge-transfer resistance determined by the reactive activity of the solid/electrolyte interface. The R_s of the CCA-Li symmetric battery is only 2.234 Ω smaller than that of pure Li (4.425 Ω) indicating a better conductivity of the LCL-bottom electrode than that of the Li electrode. This is because the unique structural characteristics of CCA (multi-dimensional conductive pathways, large specific surface area, and strong adsorption of electrolyte) provide numerous Li deposition sites. Meanwhile, the serried conductive electron pathways of CCA results in a large local current, and consequently, Li is deposited more easily. The high probability site of Li deposition is at the anode/current collector interface of the LCL-bottom electrode.

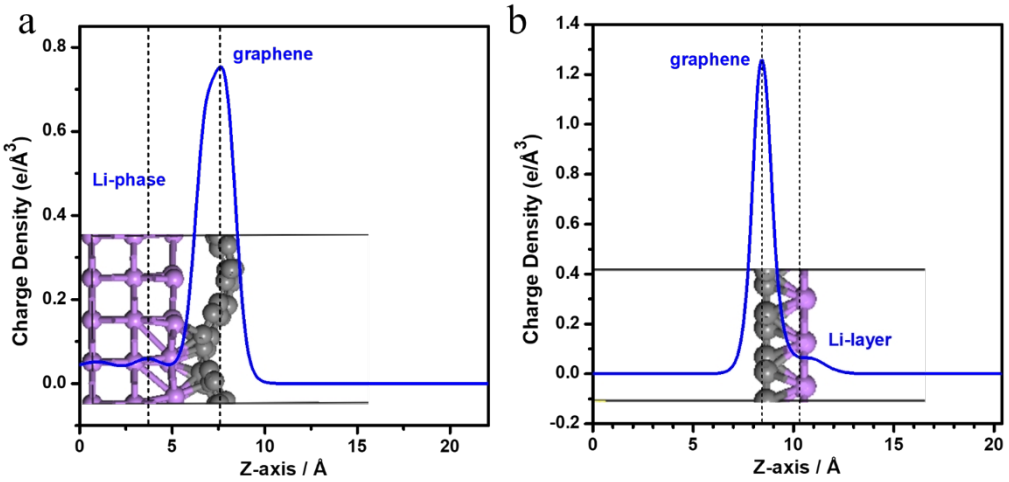

Figure S19. DFT-calculated plane-averaged charge density. **(a)** Li-graphene (LCL-interlayer) and **(b)** graphene-Li (LCL-bottom). Color code: purple, Li; gray, C.

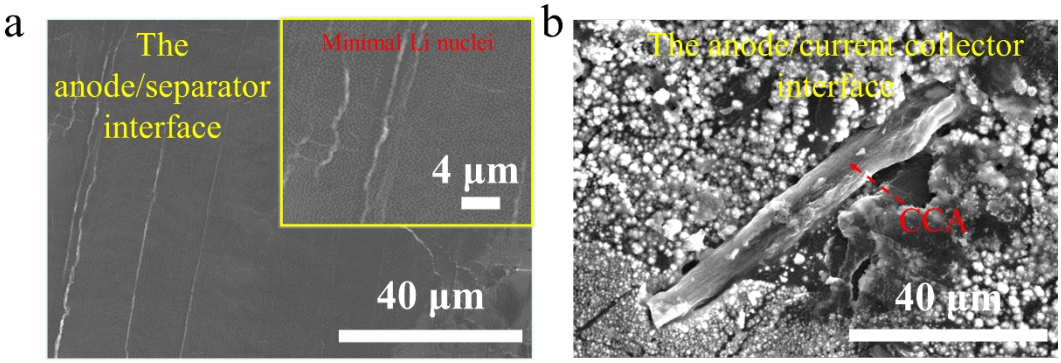

Figure S20. The SEM images about nucleation at the beginning of Li deposition. (A) The anode/separator interface of LCL-bottom, and local magnification image. (B) The anode/current collector interface of LCL-bottom. Li ions get electron on the surface of a current collector, forming the larger nuclei at the anode/current collector interface of LCL-bottom, as well as the minimal Li nuclei at the anode/separator interface.

Table S3. The density of carbon composite aerogel with a diameter of 13.8 mm.

Sample	Quality (g)	Thickness (cm)	Density (g/cm^3)
Carbon composite aerogel	0.00593	0.14	0.028
Remark		$\rho = \frac{m}{V}$	

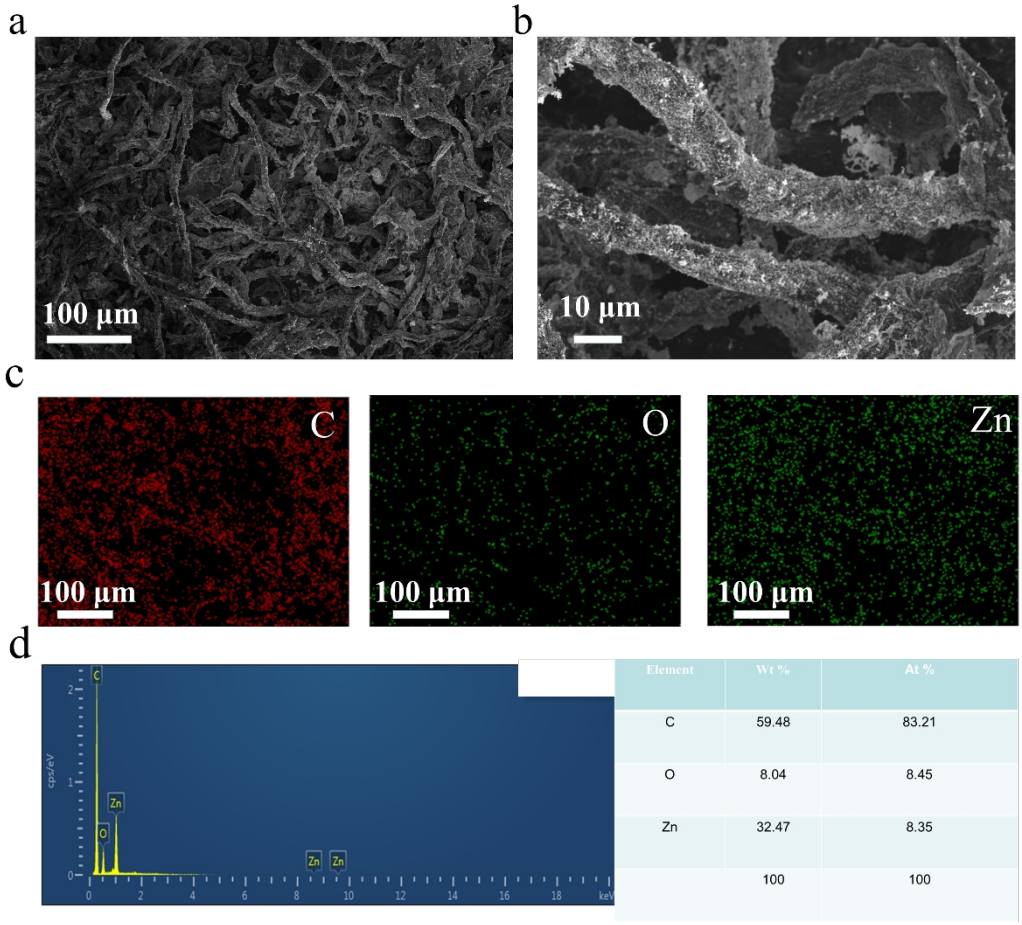

Figure S21. The Basic characterization of CCA@ZnO composite materials. (a, b) FESEM images of CCA@ZnO. **(c)** The C, O and Zn mapping of CCA@ZnO. **(d)** The corresponding EDS spectrum.

Supplementary References

1. G. Kresse, J. Hafner, *Phys. Rev. B* **1994**, *49*, 14251-14269.
2. P. E. Blöchl, *Phys. Rev. B* 1**994**, *50*, 17953-17979.
3. J. P. Perdew, K. Burke, M. Ernzerhof, *Phys. Rev. Lett.* **1996**, *77*, 3865-3868.
4. S. Grimme, J. Antony, S. Ehrlich, H. Krieg, *J. Chem. Phys.* **2010**, *132*, 154104.
5. L. Bengtsson, *Phys. Rev. B* **1999**, *59*, 12301-12304.
6. M. Brandbyge, J. L. Mozos, P. Ordejón, J. Taylor, K. Stokbro, *Phys. Rev. B* **2002**, *65*, 165401.
7. M. A. Marques, M. Oliveira, T. Burnus, *Comput. Phys. Comm.* **2012**, *183*, 2272-2281.
8. M. V. Setten, M. Giantomassi, E. Bousquet, M. J. Verstraete, D.R Hamann, X. Gonze, Rignanese, *Comput. Phys. Comm.* **2018**, *226*, 39-54.
9. S. Smidstrup, D. Stradi, J. Wellendorff, P. A. Khomyakov, U. G. Vej-Hansen, M. E. Lee, *Phys. Rev. B* **2017**, *96*, 195309.
10. T. Ozaki, K. Nishio, H. Kino, *Phys. Rev. B* **2010**, *81*, 035116 (2010).
11. G. X. Li, Z. Liu, Q. Q. Huang, Y. Gao, M. Regula, D. W. Wang, L. Q. Chen, D. H. Wang, *Nat. Energy* **2018**, *3*, 1076-1083.
12. S. F. Liu, X. H. Xia, Y. Zhong, S. J. Deng, Z. J. Yao, L. Y. Zhang, X. -B. Cheng, X. Wang, Q. Zhang, J. Tu, *Energy Mater.* **2017**, *8*, 1702322.
13. G. Huang, J. H. Han, F. Zhang, Z. Q. Wang, H. Kashani, K. Watanabe, M. W. Chen, *Adv. Mater.* **2019**, *31*, 1805334.
14. J.F. Zhu, J. Chen, Y. Luo, S.Q. Sun, L.G. Qin, H. Xu, P. Zhang, W. Zhang, W. Tian, Z. Sun, *Energy Storage Mater.* **2019**, *23*, 539-546.
15. W. Deng, W. H. Zhu, X. F. Zhou, X. Q. Peng, Z. P. Liu, *ACS Appl. Mater. Interfaces* **2018**, *10*, 20387-20395.
16. H. L. Dai, X. X. Gu, J. Dong, C. Wang, C. Lai, S. H. Sun, *Nat. Commun.* **2020**, *11*, 643.
17. F. H. Guo, C. Wu, H. Chen, F. P. Zhong, X.P. Ai, H.X. Yang, J.F. Qian, *Energy Storage Mater.* **2020**, *24*, 635-643.
18. Y. Y. Liu, D. C. Lin, Z. Liang, J. Zhao, K. Yan, Y. Cui, *Nat. Commun.* **2016**, *7*, 10992.
19. S. F. Liu, X. H. Xia, Z. J. Yao, J. B. Wu, L.Y. Zhang, S. J. Deng, *Small Methods* **2018**, *2*, 1800035.

20. S. H. Wang, Y. X. Yin, T. T. Zuo, W. Dong, J. Y. Li, J. L. Shi, *Adv. Mater.* **2017**, 1703729.

21. Q. Song, H.B. Yan, K.D. Liu, K.Y. Xie, W. Li, W.H. Gai, *Adv. Energy Mater.* **2018**, *8*, 1800564.

22. S. F. Liu, X. H. Xia, Y. Zhong, S. J. Deng, Z. J. Yao, L. Y. Zhang, X. -B. Cheng, X. Wang, Q. Zhang, J. Tu, *Energy Mater.* **2017**, *8*, 1702322.

23. L. Liu, Y. X. Yin, J. Y. Li, N. W. Li, X. X. Zeng, H. Ye, Y. G. Guo, L. J. Wan, *Joule* **2017**, *1*, 563.

24. G. Huang, J. H. Han, F. Zhang, Z. Q. Wang, H. Kashani, K. Watanabe, M. W. Chen, *Adv. Mater.* **2019**, *31*, 1805334.

25. X. R. Chen, B. Q. Li, C. Zhu, R. Zhang, X. B. Cheng, J. Q. Huang, Q. Zhang, *Adv. Energy Mater.* **2019**, *9*, 1901932.

26. J. Y. Chen, J. Zhao, L. N. Lei, P. Li, J. Chen, Y. Zhang, *Nano Lett.* **2020**, *20*, 3403.